

Loveless et al., Surface cracks record long-term seismic segmentation of the Andean margin: Supplementary text for data repository

Crack strike statistical tests

For each crack population, we test for bimodality of strike using the statistical methods outlined by Fischer (1993) and incorporated into the methods of Jones (2006). While no single threshold criterion exists for distinguishing a bimodal population from a unimodal sample or a uniform distribution, the statistics we present in Table DR1 place some quantitative constraints on the clustering of strikes in the crack populations. For each population, we solve for the mean direction θ_i and degree of clustering κ_i for two modes ($i=1, 2$), as well as the proportion of data, α , belonging to each mode, regardless of whether or not the population is qualitatively judged to appear bimodal. We operate on length-weighted strike datasets, with each crack's contribution to the distribution of strikes weighted by its length. We define α such that $\alpha=0$ represents cracks that are equally distributed between two populations, $\alpha=-0.5$ represents a distribution in which all cracks belong to mode 1, and $\alpha=0.5$ represents a population in which all cracks belong to mode 2. A large value of κ_i indicates that the data belonging to mode i are tightly clustered about the mean direction θ_i . Thus, an “ideal” bimodal distribution is characterized by distinct values of θ_i , large values for κ_i , and $\alpha=0$. Unimodal populations show $\alpha=\pm 0.5$, and populations with large variance in strike show values of θ_i that are similar and/or values of κ_i that are small.

On the basis of these categorizations, population A is the most bimodal, with a separation between the two modes of $\sim 60^\circ$, concentrated distributions within the modes, and a nearly equal partitioning of data between the two modes (Table DR1). Populations M and P are also clearly bimodal. Population B shows similar statistics, although more cracks fall into mode 1 than mode 2. While populations C, D, and I show values $\alpha < 0.2$, there is little separation between the modal angles of populations C and I, and the cracks within population D do not show strong concentration about either of the mean modal directions. Populations E, F, G, H, J, N, O, and Q show values of α close to ± 0.5 , and most show very strong clustering about one of the modal directions, indicating that they are nearly unimodal. Populations K and L show a majority of cracks lying in mode 2, though in both populations, neither concentration factor is particularly strong. This is evident in the rose diagrams (Fig. 1), which show two modes of data but substantial angular variance within each mode.

Earthquake forward modeling strategy

We use dislocation models carried out in an elastic half-space using the boundary element code Poly3D (Thomas, 1993) to calculate the principal axes of deviatoric stress induced at the surface by the earthquakes and compare these instantaneous stress fields to the directions of permanent strain recorded by the crack populations. Because these models consider small magnitude deformation, the principal stress axes should be parallel to the principal strain axes. In other words, the cracks represent permanent strain markers that formed in response to an imposed stress. In the case of the 1995 Antofagasta and 2001 Arequipa earthquakes, we use slip distributions constrained by a joint inversion of seismic and geodetic data (Pritchard et al., 2006; Pritchard et al., 2007) to calculate the

principal coseismic surface stress axes (Figs. DR1 and DR4). For the 1868 and 1877 events (Figs. DR2 and DR3), we assume simple Gaussian slip distributions, smoothly tapering from a maximum value at the epicenter to zero slip at the rupture terminations, based on estimations from historical data (Comte and Pardo, 1991; Nishenko, 1985). In the historical models, the rake of the slip vector on each modeled fault element is such that the azimuth of the surficial projection of slip is 255° , opposite the plate convergence vector. Details of the forward model parameters are shown in Table DR2.

Earthquake modeling results

The model for the 1995 Antofagasta earthquake shows predicted opening directions reasonably consistent (20° – 30° of obliquity) with the NW mean strikes of cracks in the two populations east of the Mejillones Peninsula (Fig. DR1). We do not know whether or not cracks in either of these regions were reactivated during the earthquake. In both of clusters, we also observe a concentration of cracks striking NE (Fig. 1), oblique to the crack strikes predicted by the coseismic model. We suggest that earthquakes on the Antofagasta segment of the plate boundary can reactivate the NW striking cracks, while an earthquake on the Iquique segment, which lies directly to the north, could affect the NE striking features.

These NE striking cracks are indeed consistent with the stress field predicted for the simulated 1877 Iquique earthquake, which is inferred to have ruptured the plate boundary between the Arica bend to the Mejillones Peninsula (Fig. DR2). Near the inferred epicenter (Comte and Pardo, 1991) and locus of maximum modeled slip, crack strikes and coseismic σ_1 axes are nearly parallel to the coastline. Around 21.5°S , where a population of cracks strike dominantly NNE, the predicted principal stress axes show a

consistent clockwise rotation relative to their orientations nearer the epicenter. The four northernmost crack populations affected by seismicity on the Iquique segment show a concentration of NW strikes, consistent with the opening direction predicted by the model. Two of those regions show bimodal strike distributions, with NW and NE strikes. As in the case of the cracks near the Mejillones Peninsula, the NW striking cracks may be activated by Iquique segment seismicity, while activity on the adjacent segment to the north may dominantly drive the evolution of the NE striking features.

The 1868 earthquake ruptured a large segment of the southernmost Peru margin, with a southeastern termination estimated to coincide with the large bend in the plate boundary and coastline (Comte and Pardo, 1991; Nishenko, 1985) (Fig. DR3). The rupture area of the 1604 great earthquake is estimated to be very similar to that of the 1868 event (Comte and Pardo, 1991; Keefer and Moseley, 2004). As postulated above, the σ_1 axes induced by the 1868 earthquake in northernmost Chile trend NE-SW, consistent with the NE striking cracks that we observe in two populations in that region, while the NW striking cracks are not strongly influenced by the static stress related to the southern Peru earthquakes.

Crack-based inversion strategy

We use Poly3DInv (Maerten et al., 2005) to invert the strain fields demonstrated by the surface cracks for the slip on the subduction thrust. This boundary element program allows use of strain tensor data to constrain the distribution of slip on the subduction interface. We assign a principal strain tensor to each of the 16 crack populations within the bounds of the 1877 earthquake segment, with the principal axis orientations reflecting the mean strike of cracks in the cluster and the principal strain

magnitudes representing the amount of finite strain exhibited by cracks. Where cracks show a bimodal distribution in strike, we selectively filter the crack population such that the mean strike used in the inversion reflects only the set more favorably oriented for opening according to the predictions of the simple Gaussian slip forward model. In some models, we define the strain magnitude by calculating the mean crack density (total length of cracking per unit area) in each population, while in others, we assign a uniform strain magnitude to all crack clusters. The crack density-based strain magnitude is equal to the mean of the total length of cracking within 90 m resolution cells throughout each crack population divided by the area of each grid cell, to yield crack density in m/m^2 or m^{-1} . The range of this value amongst all 16 crack populations is $0.058\text{--}0.124 \text{ m}^{-1}$. We convert the crack density to strain magnitude by modulating the density value by an exponent. Test inversions of the crack dataset indicated that multiplying crack density by 10^{-5} , yielding strain magnitudes of $5.8 \times 10^{-7} - 1.24 \times 10^{-6}$, resolved maximum slip values of ~ 7 m, with an overall moment magnitude of 8.5. This is similar to the estimates of maximum slip and moment for the 1877 earthquake (Nishenko, 1985). For the uniform strain models, we chose a magnitude of 1×10^{-6} , which resolved a maximum slip value of 8 m and moment magnitude of 8.5, also reasonably consistent with the estimated parameters. In addition to solving for the slip distribution, we estimate remote deviatoric strain and stress tensors; the coseismic strain plus this remote tensor theoretically sums to the input strain constrained by the cracks.

Poly3DInv permits multiple constraints to be applied during the inversion, including simultaneously minimizing the misfit between model and data and the roughness of the slip distribution, and limiting the sense of strike- and dip-slip to a

specified direction through use of a weighted, constrained least-squares inversion (Maerten et al., 2005; Menke, 1984). In all of our inversions, we restrict the dip and strike slip to be reverse and left-lateral, respectively, consistent with the direction of plate convergence. Furthermore, we prohibit slip on the elements that line the edges of the modeled fault.

We carry out a series of inversions with varying parameters to investigate which resolved properties of the slip distribution are most robust. All modeling assumes a known subduction thrust geometry which we constructed by fitting a three-dimensional curved surface to the Wadati-Benioff zone contours of Cahill and Isacks (1992) between depths of 0 km (trench) and 75 km, then discretized with triangular elements in order to retain the along-strike and down-dip curvature. We test the effects of a) uniform versus density-weighted strain magnitude, b) subsampling the crack data, c) resolving the slip distribution onto a fine and coarse mesh of triangular elements, d) applying different smoothing factors to the resulting slip distribution, e) adding an artificial data point in the gap in crack observations between 21.5° and 22.5°S to see whether the pattern of slip resolved around that latitude is affected by the lack of local data, and f) testing the effects of imposed remote stress.

We group the inversions in four subsets based on permutations of two parameters: use of crack density-weighted strain magnitudes versus identical strain magnitudes at each cluster (“u” suffix in Table DR3), and use of a coarse fault mesh versus a denser mesh (“d” suffix in Table DR3). For each of the four combinations of variable/uniform strain magnitudes and coarse/dense meshes, we generate a model using four subsets of the constraining data. One model in each group uses the mean strike of all crack

populations (“A” prefix in Table DR3), while the three other models use subsets of the data, excluding information from up to 7 of the 16 clusters (“B1,” “B2,” or “B3” prefix in Table DR3). These subsets were chosen to eliminate closely spaced observations with substantially different mean strike values (B1 and B2) or to distribute more evenly the control points along the coastline (B3). However, the lack of any crack population between 21.5° and 22.5°S limits the resolution of slip within those bounds. As mentioned in the main text, high topography in this region impedes development of the gypsum-indurated sediment crust, which plays a key role in crack preservation. Therefore, coseismic stress fields in this segment are likely capable of producing and reactivating cracks, but the lack of a durable surface crust prevents their long-term preservation. We test the effects of this data gap by generating models with an artificial data point that constrains deformation in this region.

Inversion results

We use the resolved slip distributions to calculate the principal stress axes at each crack population location, as in the case of the forward models. Before carrying out this forward modeling, we scale the resolved earthquake slip such that the maximum slip magnitude is 8 m, roughly consistent with the maximum value estimated for the 1877 earthquake (Comte and Pardo, 1991; Nishenko, 1985). The gradient of slip – and therefore the calculated orientations of principal stress at the surface – does not change as a result of this modification. We evaluate the goodness-of-fit of each inverse model by calculating the angular difference between the mean crack strike observed within each cluster and the most-compressional principal stress (σ_1) axis calculated at the cluster location. As mentioned in the main text, the strike of a mode 1 crack is parallel to the σ_1

direction of the deviatoric stress field that created it. We calculate the minimum, maximum, and mean angular difference between the observed and predicted crack strike, and we summarize the overall model misfit by summing the angular discrepancies between model and data for all crack populations (Table DR3).

There are several fundamental differences between the models. For all permutations of geometry and data subsets, the slip distributions constrained using a uniform strain magnitude for all crack locations produce a stress field that better fits the observations than the corresponding model that used the variable, crack density-based strain magnitudes. The mean slip azimuth, defined as the mean surficial projection of the element slip vector, weighted by slip magnitude, is consistently rotated southwest from the expected direction opposite the plate convergence azimuth of 255° (Table DR3). Inversions of the full crack dataset resolve a mean slip vector closest to this expected value, while use of subset 1 results in slip vectors with a stronger sinistral component than expected.

All model parameter permutations resolve maximum slip in a region between 19° and 21°S (e.g., Fig. 3), with variations between models in the exact locus of maximum slip. Secondary patches of slip are concentrated around the southern extent of the modeled fault region (23°S) in all models except B1 variants, which show patches of slip around 22°S . The differences in resolved slip pattern between the coarse and fine mesh models, as well as the uniform and density-based strain magnitude models, are slight. Adding the artificial crack population within the gap in crack-based strain data results in a negligible change to the resulting slip distributions. Enhancing the smoothing of the slip distribution – that is, minimizing the curvature of the slip magnitude between

adjacent triangular elements, serves to change the slip distribution in a predictable manner: models subject to more smoothing show a more broadly distributed pattern of slip than those with a lesser degree of smoothing.

Estimate of remote stress and its effects

Unlike in a geodetic inversion, where a displacement field is used to estimate the distribution of slip during a portion of the seismic cycle, the formation of cracks – our constraining data – depends not only on the changes induced by the seismic cycle, but also the initial conditions. That is, a geodetic displacement or velocity field simply represents a change in state that is independent of the initial condition. Conversely, in order to create forearc cracks, the deviatoric stress induced by a tectonic perturbation (e.g., an earthquake) must be favorably oriented and sufficiently large to counteract the existing state of stress in the rock. In a subduction zone, this remote or regional deviatoric stress reflects the effects of long-term processes acting on the forearc, such as plate boundary forces (slab pull and ridge push), tectonic erosion processes, and gravitational stresses due to the adjacent orogenic plateau (e.g., Richardson and Coblenz, 1994; Wdowinski and O'Connell, 1991).

We simultaneously solve for the earthquake slip distribution and remote strain and deviatoric stress tensors as part of our inversion routine (Maerten et al., 2005). This procedure only estimates the remote values for the region in which the cracks lie; the solution comprises the best-fitting remote tensors and slip distribution that sum to give the input data. Because the input data represent deformation, they place constraints only on the deviatoric part of the stress tensor, that is, the portion of the stress tensor capable of driving non-volumetric deformation (Jaeger and Cook, 1976). The orientations of the

principal estimated remote stress and strain axes are consistent with the tectonic setting of a forearc, with axes of greatest principal compression directed approximately parallel to plate convergence with magnitude $\sim 6.5 \times 10^4$ Pa – about 0.1-0.5 times the calculated coseismic values calculated at the surface in coastal regions of the forearc. To demonstrate the effects of the remote stress, we plot the principal deviatoric stress axes for the approximate forward model of the Iquique earthquake (e.g., Fig. DR2) for four cases: neglecting remote stress (Fig. DR5a), considering the remote stress estimated in our preferred inversion (6.5×10^4 Pa principal deviatoric compression directed 070° , 1×10^4 Pa principal deviatoric tension directed 340° , Fig. DR5b), a remote stress oriented identically to that estimated by the preferred inversion, but with magnitude ten times greater (6.5×10^5 Pa principal compression directed 070° , Fig. DR5c), and a case of 100 times the estimated magnitude (6.5×10^6 Pa principal compression directed 070° , Fig. DR5d). In the interior of the forearc, east of the crack distribution, as well as to the north and south of the crack distributions likely affected by seismicity on the Iquique segment, the magnitude of the principle coseismic deviatoric stresses are comparable to 10 times the estimated remote magnitude (Fig. DR5c). Thus, if cracks were to form in that region, their orientations would be determined by both the coseismic and remote stress fields. When remote stress of magnitude 100 times that estimated from the inversion is imposed on the model (Fig. DR5d), it dominates the stress field such that the earthquake plays little role in dictating potential crack orientations; the principal stress axes everywhere are very similar in magnitude and orientation to those of the remote stress tensor. Thus, we suggest that a regional deviatoric stress tensor with principal compression of $\sim 5 \times 10^5$ Pa or less directed parallel to plate convergence is consistent with our observations. In this

scenario, the stresses induced by great subduction zone earthquakes modulate the regional stresses and give rise to the large-scale, systematic variations in principal stress orientations that are manifest in the crack strikes. The magnitudes of our remote stress values are 1-2 orders of magnitude smaller than the absolute compression calculated by Richardson and Coblenz (1994) for the Andean orogen, but we reiterate that the crack data we use to constrain stress values provide information only about the deviatoric part of the total stress tensor. Nonetheless, our estimated remote stress is low magnitude and requires that the magnitudes of the absolute principal stresses are nearly equal.

Some modifications to our model could be made that would increase the estimated remote stress. First, we could increase the exponent chosen to represent the magnitude of strain values used as input to the inversion. Test models with an exponent of 10^{-5} result in unrealistically high magnitude slip (45 m, with the maximum slip occurring at the NW corner of the fault) and predicted earthquake size ($M_w=9$). The remote stress estimated from such a test is on the order of 1 MPa, which is more consistent with the previous regional studies, but the slip distribution is unreasonable. We could introduce further complexity into the model and consider a spatially variable exponent of input stress magnitude, but we prefer to keep the input magnitude parameters as simple as possible given their poor constraint relative to the stress orientations.

Finally, we note the results of Taylor et al. (1998), who found that the style of upper plate seismicity in a subduction zone depends on the distribution of coupling on the subduction zone interface, in addition to the time since the last subduction zone earthquake. Their results found correlation between the shear stress induced in the upper plate by a subduction zone earthquake and the mechanisms of strike-slip earthquakes

(aftershocks). The parameters used in their studies suggest that the spatial variability of slip on the plate interface, namely the presence, extents, and abrupt terminations of asperities, predicts the distribution of upper plate stress and therefore orientations of aftershocks. While Taylor et al. (1998) do not specifically mention the effect of remote stresses on their simulations, the correlation between the orientation of failure shown by aftershocks with the sense of coseismically induced stress shows a similar result to that which we present here, at least for the case of reactivated surface cracks.

Effect of slip gradient on stress field

We find that the stress pattern predicted by the various inverse model permutations is relatively insensitive to the details of the slip distribution. Rather, the actual limits of the rupture area seem to exert the greatest influence over the stress exerted on the forearc. We demonstrate this effect in Fig. DR6, which shows the effect of varying interplate slip gradients on the azimuth of maximum principal tension (σ_3 , perpendicular to crack strike) at the surface. To construct these figures, we apply a Gaussian slip distribution, varying smoothly from unit thrust slip at the center of a fault (of length L , downdip extent $W=L/2$, and dip 10° , breaking the surface at $x = 0$) to zero at the edges. The along-strike location of the maximum slip magnitude is located at $y = L/2$ in the top row of Fig. DR6 and $y = 3L/4$ in the bottom row of Fig. DR5; in both cases, the maximum slip occurs at a downdip location of $W/2$. The azimuth of σ_1 is calculated from $y = -3L/2$ to $3L/2$ along a strike-parallel line located at $x \sim 3L/7$ from the updip extent of the fault. With decreasing slip concentration, shown from left to right in Fig. DR5, the latitudinal change in σ_3 trend becomes less sinusoidal and more linear. This change in pattern is subtle, indicating that it is difficult to uniquely relate the details of the slip

distribution to surface data constraining the pattern of stress axes. However, these simple models show that the general pattern of σ_3 azimuth is strongly dependent on the actual extents of the rupture, with σ_3 oriented approximately perpendicular to the slip vector around the extremes of rupture zone and nearly parallel to the rake around the center of the slipping region.

Dynamic stress modeling

As mentioned in the main text, we use the method of Cotton and Coutant (Cotton and Coutant, 1997) in conjunction with the spatiotemporal evolution of slip related to the 1995 Antofagasta (Pritchard et al., 2006) and 2001 Arequipa (Pritchard et al., 2007) earthquakes to calculate the dynamic stress field related to these events. We note good agreement between the orientations of the principal stress axes throughout the time series with the corresponding orientations of the static stress solution. This is demonstrated by Fig. DR7, which shows three rose diagrams illustrating consistency between the angular distribution of σ_1 throughout the time series with the static σ_1 orientation.

Figure captions

Figure DR1. Static principal coseismic stress axes resulting from the 1995 M_w 8.1 Antofagasta earthquake on the Andean subduction interface. The distribution of slip is based on a joint inversion of seismic, GPS, and InSAR data (Pritchard et al., 2006). The gray lines show the most compressional principal stress axes (σ_1); the least compressional (σ_3) axes are omitted for clarity but are oriented perpendicular to σ_1 . The red bars show the mean strike of cracks within a particular cluster. In this case, the bimodal crack distributions were filtered and the orientation shown represents the mean of only the northwest-striking cracks. The blue bars show the model-predicted orientation of σ_1 at

the locality of the crack populations, which represents the strike of the mode 1 crack that would theoretically open in response to the coseismic stress field.

Fig. DR2. Static principal coseismic stress axes resulting from the 1877 $M \sim 8.5$ Iquique earthquake on the Andean subduction interface. The distribution of slip is approximated based on historical estimation of the epicenter and maximum slip (Comte and Pardo, 1991; Nishenko, 1985) and not on our inverse model (Fig. 4 of the main text). All symbols are as described in Fig. DR1.

Figure DR3. Static stress model for the 1868 $M \sim 8.5$ earthquake in southern Peru. The slip distribution is approximated based on the rupture extent and magnitude estimates (Comte and Pardo, 1991; Nishenko, 1985). All symbols are as described in Fig. DR1.

Figure DR4. Static stress model for the 2001 M_w 8.5 Arequipa, Peru earthquake. The slip distribution is based on a joint inversion of seismic, GPS, and InSAR data (Pritchard et al., 2007). The symbols are as described in Fig. DR1.

Figure DR5. Plots showing the effect of remote or regional deviatoric stress on the principal stress axes along the Iquique segment of the margin. a) Calculated σ_3 axes for the approximate model of the 1877 Iquique earthquake (e.g., as shown in Fig. DR2) with no remote stress considered. b) Calculated σ_3 axes for the Iquique event considering the remote deviatoric stress estimated in our preferred inversion (σ_1 of 6.5×10^4 Pa directed 070° , σ_1 of 1×10^4 directed 340°). c) and d) Calculated σ_3 axes considering a remote stress whose principal axes are oriented the same as in b), but with magnitude 10 (c) and 100 (d) times greater. Even when increasing the magnitude of remote stress to 10 times that estimated by the inversion, the orientations of principal stress axes near the coast, where the crack are concentrated, are negligibly affected. Near the northern and southern ends

of rupture, as well as in the inner forearc, coseismic stresses are smaller and therefore these axes are affected by the remote stress. A remote stress magnitude 100 times that estimated for the crack dataset dominates the stress field such that the coseismic stress plays little role in dictating predicted failure planes.

Figure DR6. Plots showing the effect of slip gradient on minimum principal stress axis azimuth. The gray Gaussian curve shows the degree of along-strike concentration of slip applied to a shallowly dipping fault, while the solid black line shows the azimuth of the σ_3 axes calculated at the surface along a line parallel to the fault located above its downdip extent. For both the cases in which the slip pulse is located in the center of the fault (top row) or shifted off-center (bottom row), the azimuth of the least compressional stress axis is more sensitive to the location of the boundaries of the rupture, defined by the gray box, than to the details of the slip distribution.

Figure DR7. Dynamic stress effects of the 1995 Antofagasta earthquake. Shown as gray bars throughout the affected region are the static σ_1 axes, as initially presented in Fig. DR1. The three rose diagrams show the distribution of σ_1 orientations at a given locality, calculated at 0.5 second intervals throughout the first 100 seconds of the rupture, while the bold arrow in each diagram indicates the trend of the static σ_1 axis at that locality. The similarity between the temporal distribution of σ_1 orientation and the static direction indicate that the direction of dynamic stress induced throughout the rupture is similar to the static stress effects.

References

- Cahill, T.A., and Isacks, B.L., 1992, Seismicity and shape of the subducted Nazca Plate: *Journal of Geophysical Research*, v. 97, p. 17,503-17,529.
- Comte, D., and Pardo, M., 1991, Reappraisal of great historical earthquakes in the northern Chile and southern Peru seismic gaps: *Natural Hazards*, v. 4, p. 23-44.
- Cotton, F., and Coutant, O., 1997, Dynamic stress variations due to shear faults in a plane-layered medium: *Geophysical Journal International*, v. 128, p. 676-688.
- Fischer, N.I., 1993, *Statistical Analysis of Circular Data*: New York, Cambridge University Press, 277 p.
- Jaeger, J.C., and Cook, N.G.W., 1976, *Fundamentals of Rock Mechanics*: New York, Halsted Press, 585 p.
- Jones, T.A., 2006, MATLAB functions to analyze directional (azimuthal) data-I: Single-sample inference: *Computers & Geosciences*, v. 32, p. 166-175.
- Keefer, D.K., and Moseley, M.E., 2004, Southern Peru desert shattered by the great 2001 earthquake: Implications for paleoseismic and paleo-El Niño-Southern Oscillation records: *Proceedings of the National Academy of Sciences*, v. 101, p. 10878-10883.
- Maerten, F., Resor, P., Pollard, D.D., and Maerten, L., 2005, Inverting for slip on three-dimensional fault surfaces using angular dislocations: *Bulletin of the Seismological Society of America*, v. 95, p. 1654-1665.
- Menke, W., 1984, *Geophysical data analysis: Discrete inverse theory*: New York, Academic Press, 289 p.
- Nishenko, S.P., 1985, Seismic potential for large and great interplate earthquakes along the Chilean and southern Peruvian margins of South America: A quantitative reappraisal: *Journal of Geophysical Research*, v. 90, p. 3589-3615.
- Pritchard, M.E., Ji, C., and Simons, M., 2006, Distribution of slip from 11 $M_w > 6$ earthquakes in the northern Chile subduction zone: *Journal of Geophysical Research*, v. 111, B10302, doi:10.1029/2005JB004013.
- Pritchard, M.E., Norabuena, E.O., Ji, C., Boroschek, R., Comte, D., Simons, M., Dixon, T., and Rosen, P.A., 2007, Geodetic, teleseismic, and strong motion constraints on slip from recent southern Peru subduction zone earthquakes: *Journal of Geophysical Research*, v. 112, B03307, doi:10.1029/2006JB004294.
- Richardson, R.M., and Coblentz, D.D., 1994, Stress modeling in the Andes: Constraints on the South American intraplate stress magnitudes: *Journal of Geophysical Research*, v. 99, p. 22015-22025.
- Taylor, M.A.J., Dmowska, R., and Rice, J.R., 1998, Upper plate stressing and seismicity in the subduction earthquake cycle: *Journal of Geophysical Research*, v. 103, p. 24523-24542..
- Thomas, A.L., 1993, *Poly3D: A Three-Dimensional, Polygonal Element, Displacement Discontinuity Boundary Element Computer Program with Applications to Fractures, Faults, and Cavities in the Earth's Crust [M.S. thesis]*: Palo Alto, CA, Stanford University.
- Wdowinski, S., and O'Connell, R.J., 1991, Deformation of the central Andes (15°-27°S) derived from a flow model of subduction zones: *Journal of Geophysical Research*, v. 96, p. 12245-12255.

Figure DR1

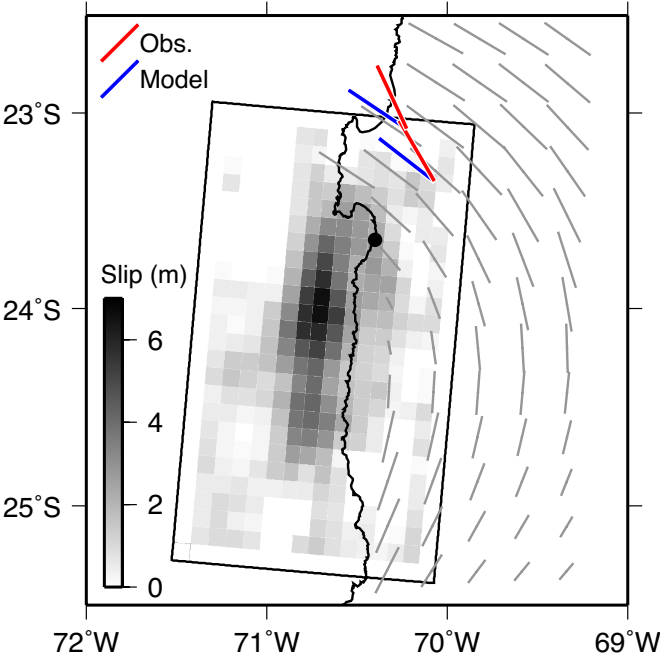


Figure DR2

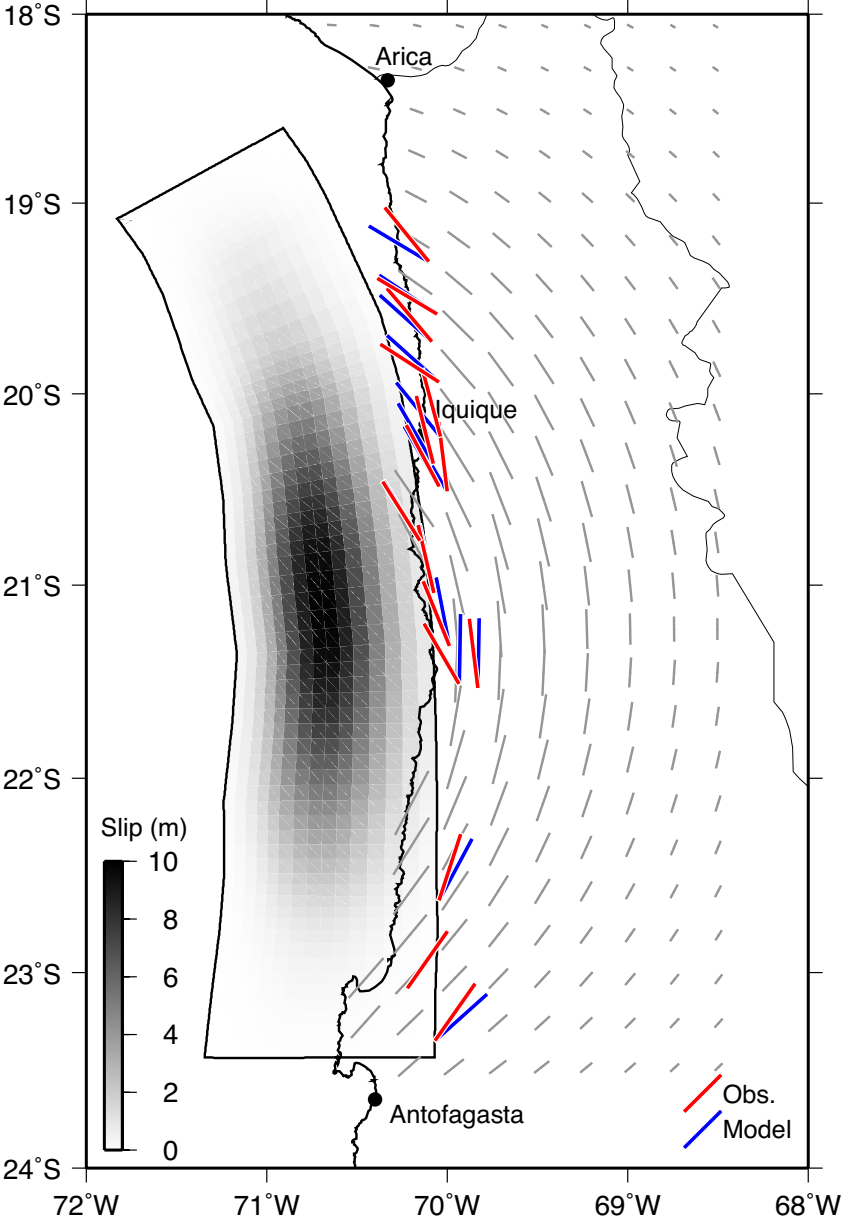


Figure DR3

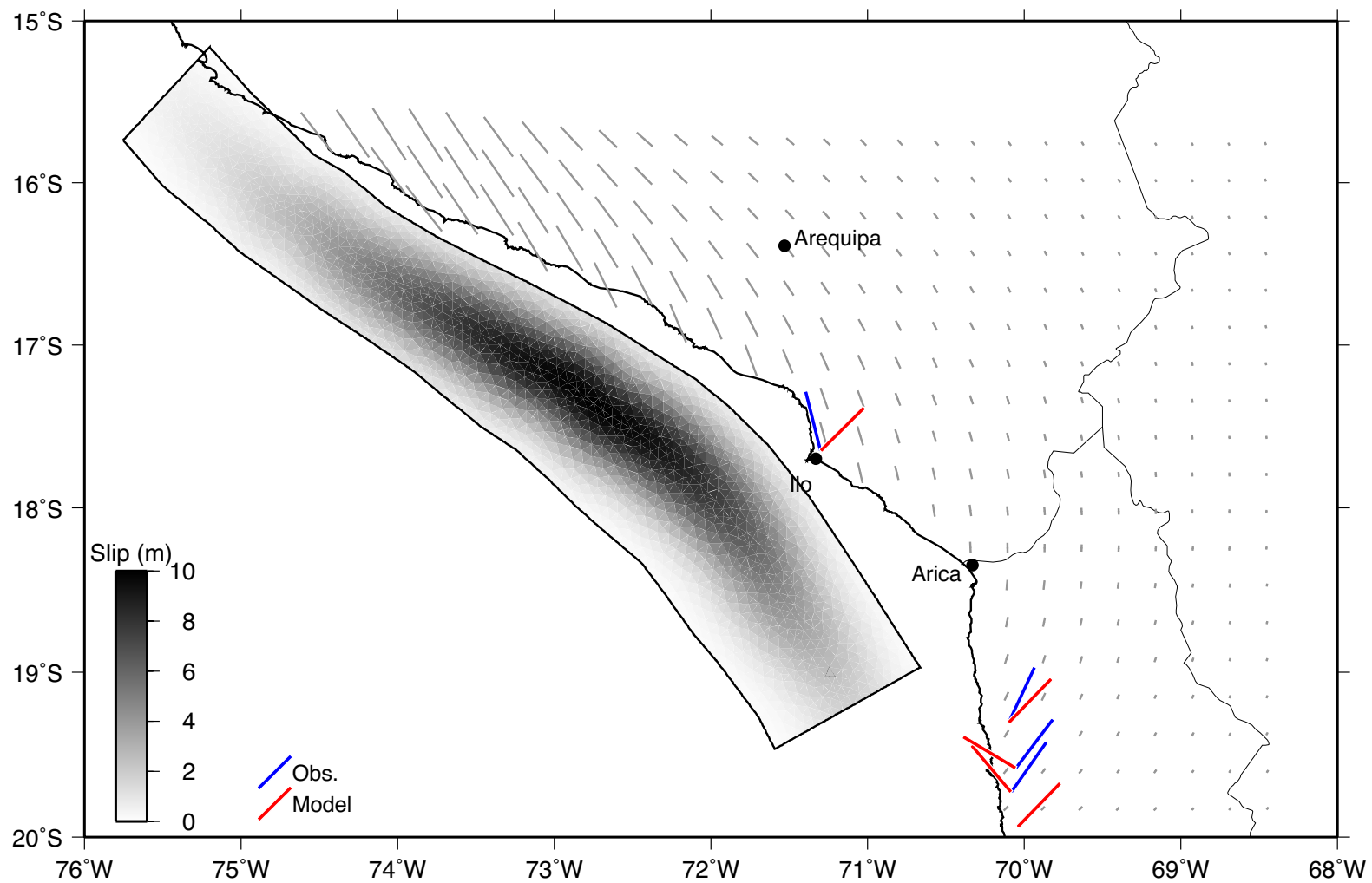
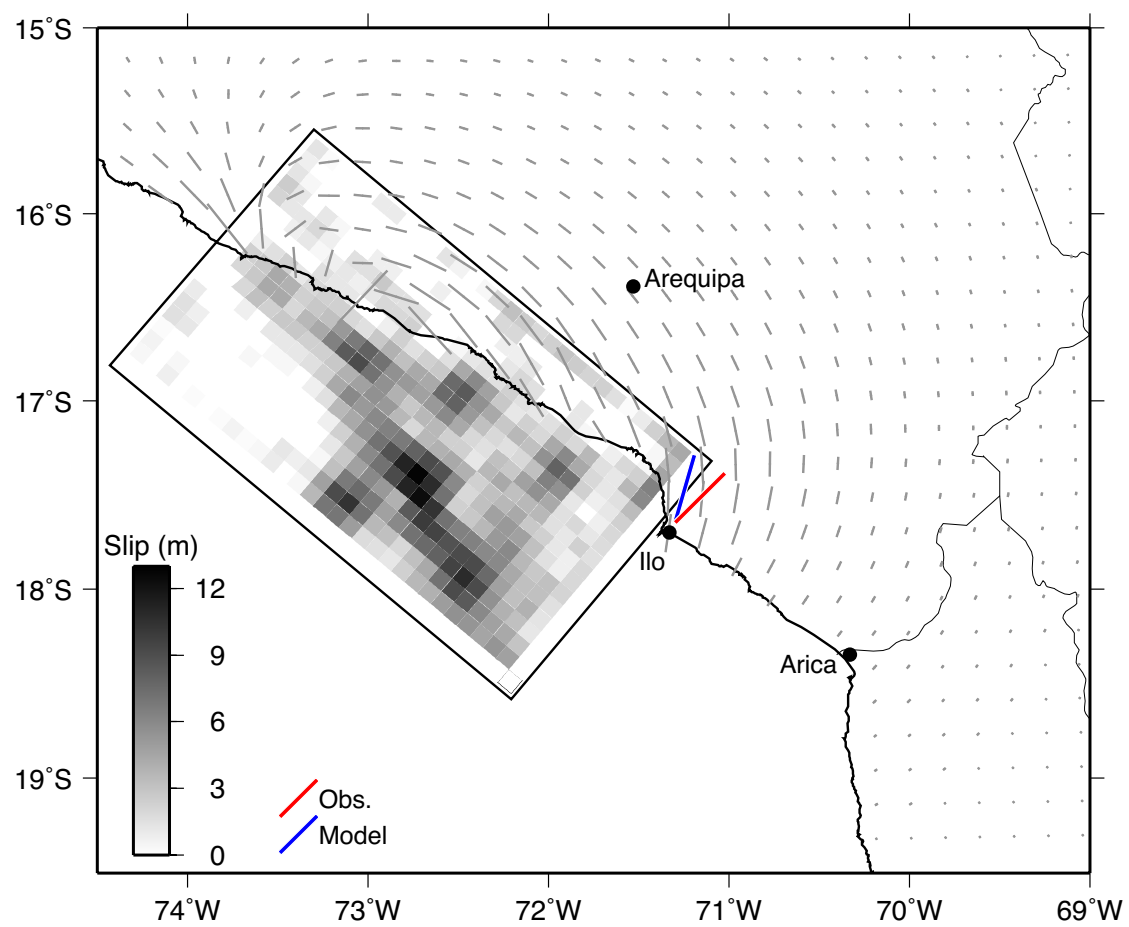


Figure DR4



Loveless Fig. DR5

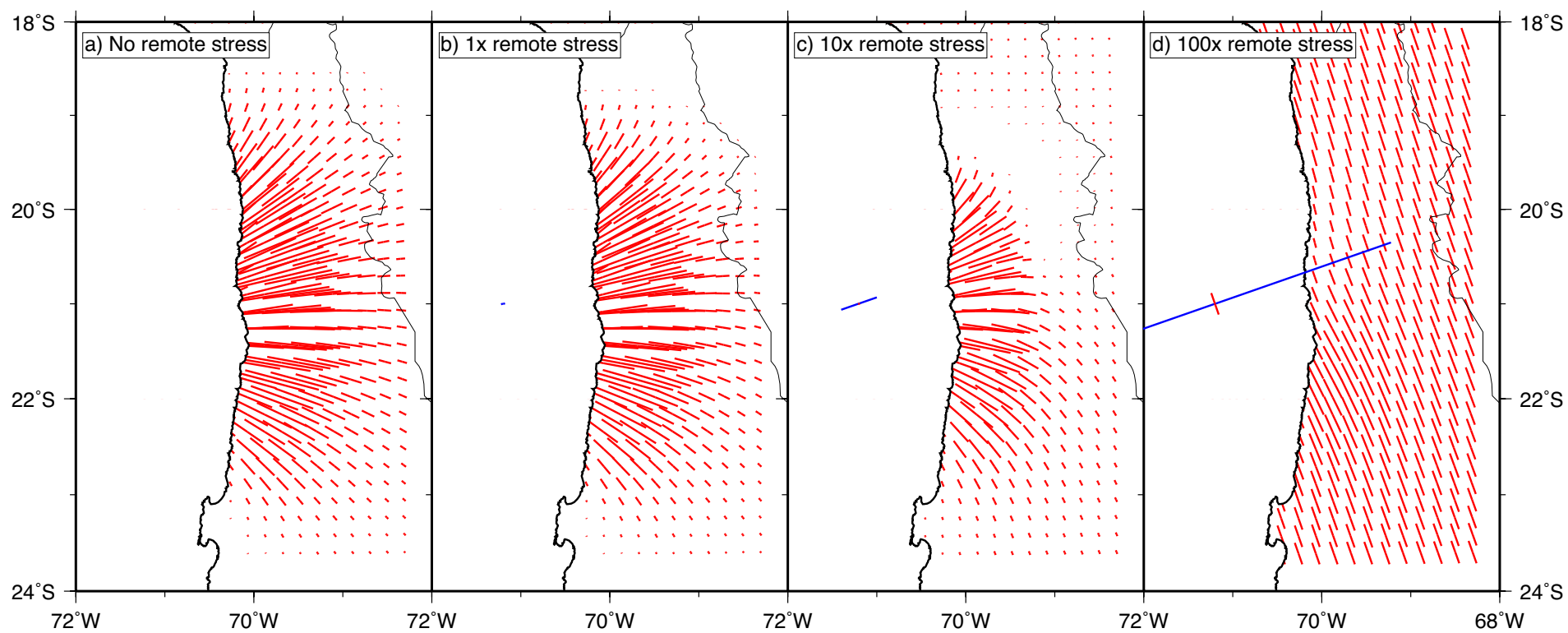


Figure DR6

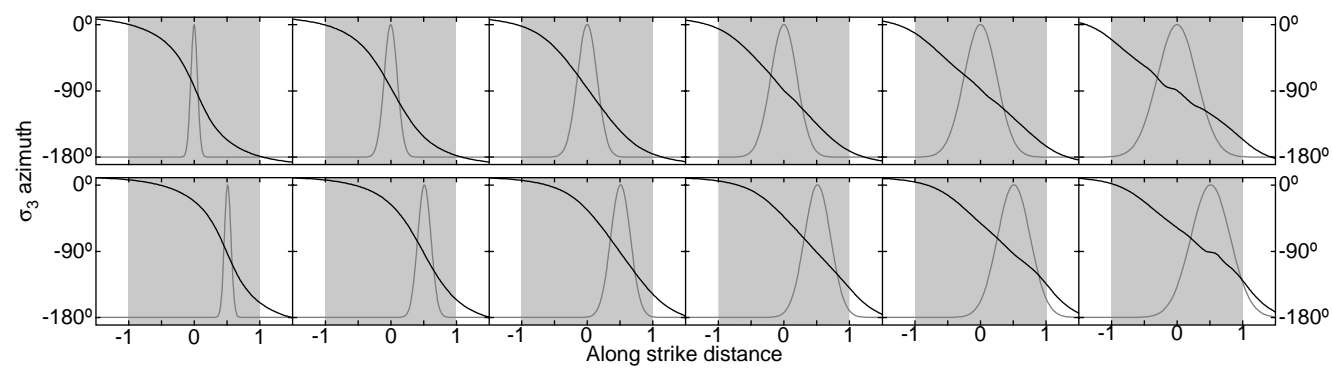


Figure DR7

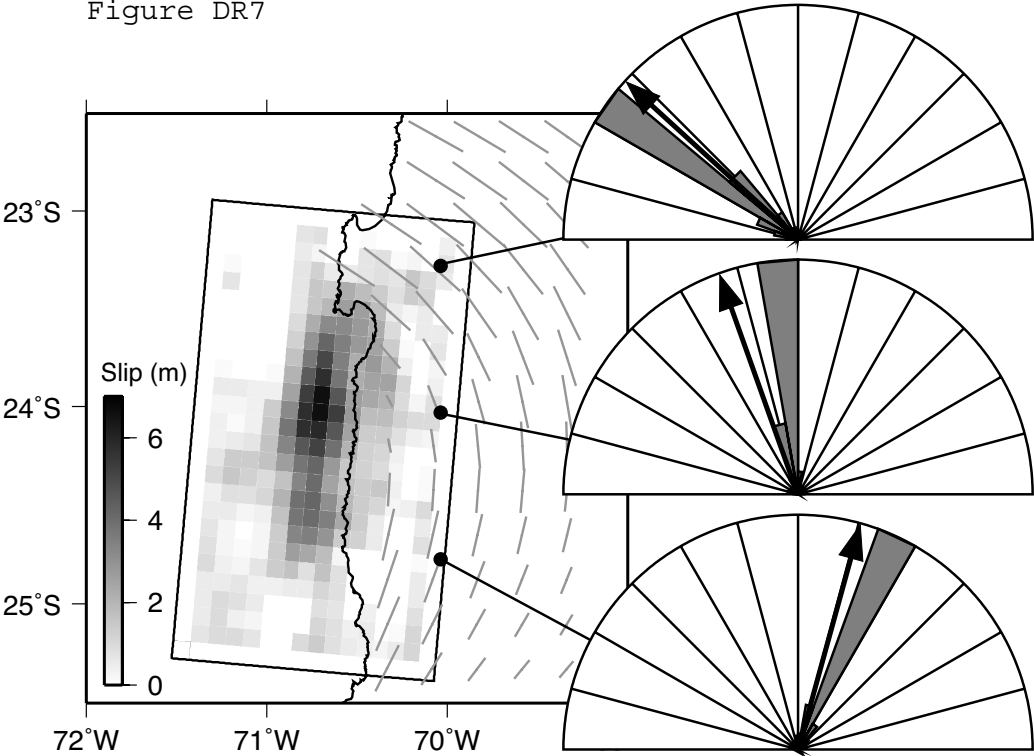


Table DR1. Statistics of crack strike bimodality.

Label on Fig. 1	Latitude	θ_1^\dagger	κ_1^\ddagger	θ_2^\dagger	κ_2^\ddagger	α^\S	Bimodal
A	-23.35	31.2	6.06	331.7	9.81	-0.01	Y
B	-23.08	31.5	3.70	339.9	16.04	-0.17	Y
C	-22.63	24.3	12.15	360.0	1.39	-0.12	N
D	-21.54	22.8	2.42	335.5	3.05	0.12	N
E	-21.52	26.9	1.34	327.9	4.73	0.45	N
F	-21.32	66.4	5.79	328.7	3.63	0.37	N
G	-21.04	45.4	4.18	332.4	4.68	0.25	N
H	-20.77	70.7	7.44	318.3	5.45	0.37	N
I	-20.51	15.4	2.71	345.0	12.40	0.19	N
J	-20.49	12.8	2.17	328.5	9.48	0.38	N
K	-20.37	23.9	5.35	330.3	4.63	0.20	Y
L	-20.23	59.9	7.88	344.7	3.10	0.20	Y
M	-19.94	37.6	5.84	300.4	19.22	0.12	Y
N	-19.73	16.5	0.93	318.7	16.04	0.45	N
O	-19.58	0.0	0.55	299.7	21.54	0.45	N
P	-19.31	45.9	6.66	330.2	3.54	-0.08	Y
Q	-17.65	57.7	8.91	305.7	3.46	-0.31	N

$^\dagger \theta_i$ denotes the mean direction of the mode.

$^\ddagger \kappa_i$ denotes the concentration of data about θ_i (larger κ_i is more concentrated).

$^\S \alpha$ indicates the degree to which the data are partitioned into the two modes. An α value of 0 means that the data are equally partitioned into the two modes, an α value of -0.5 indicates that all data belong to mode 1, and an α value of +0.5 indicates that all data belong to mode 2.

Table DR2. Earthquake forward modeling parameters.

Event	Moment (N-m) [†]	Moment magnitude	Dimensions (km) [‡]	Mean slip (m)	Max. slip (m)	Mean rake [§]
1868	6.6×10^{21}	8.5	625 × 125	3.18	9.98	54
1877	4.2×10^{21}	8.3	530 × 135	1.90	9.85	105
1995	1.2×10^{21}	8.0	210 × 160	0.94	6.58	105
2001	4.0×10^{21}	8.3	320 × 210	2.19	12.80	69

[†] Moment is defined as the modulus of rigidity (3×10^{10} N/m²) times the sum of the slip times area of all fault patches.

[‡] Rupture dimensions, shown as along-strike × down-dip dimension.

[§] Mean of rake on all fault patches, weighted by slip magnitude. 0° = left-lateral slip, 90° = reverse slip, ±180° = right-lateral slip, -90° = normal slip.

Table DR3. Crack-based inversion parameters.

Model [†]	N _E [‡]	Moment (N-m) [§]	M _w	Slip (m)		Slip az. [#]	Angular error ^{††}			
				Mean	Max.		Min.	Max.	Mean	Total
A	369	6.3×10^{21}	8.5	2.1	8.0	242	0.2	75.1	18.2	291
B1	369	3.0×10^{21}	8.2	0.9	8.0	199	7.6	63.9	34.4	550
B2	369	3.0×10^{21}	8.3	1.0	8.0	229	0.1	68.0	19.0	304
B3	369	2.2×10^{21}	8.2	0.7	8.0	213	2.8	75.7	26.9	430
Au	369	6.8×10^{21}	8.5	2.3	8.0	239	0.3	30.3	13.1	210
B1u	369	3.4×10^{21}	8.3	1.1	8.0	204	4.1	43.0	18.3	293
B2u	369	3.7×10^{21}	8.3	1.2	8.0	224	0.4	28.4	9.0	144
B3u	369	2.3×10^{21}	8.2	0.7	8.0	228	6.7	72.1	23.4	374
Ad	1009	8.9×10^{21}	8.6	2.9	8.0	237	0.8	59.5	15.8	253
B1d	1009	4.3×10^{21}	8.4	1.4	8.0	192	0.8	49.4	15.1	242
B2d	1009	3.5×10^{21}	8.3	1.1	8.0	225	2.5	56.2	20.3	325
B3d	1009	2.3×10^{21}	8.2	0.7	8.0	235	3.3	48.8	21.0	336
Adu	1009	6.2×10^{21}	8.5	2.0	8.0	240	0.4	33.4	13.5	217
B1du	1009	5.3×10^{21}	8.4	1.8	8.0	205	3.2	40.7	15.0	241
B2du	1009	3.8×10^{21}	8.3	1.2	8.0	218	0.3	27.5	11.3	181
B3du	1009	3.5×10^{21}	8.3	1.1	8.0	229	8.6	43.5	18.8	300
Adux	1009	7.0×10^{21}	8.5	2.3	8.0	235	0.9	44.1	15.3	260
B1dux	1009	5.4×10^{21}	8.4	1.8	8.0	198	1.2	43.6	17.4	295
B2dux	1009	4.0×10^{21}	8.3	1.3	8.0	222	1.2	26.1	12.5	213
B3dux	1009	4.6×10^{21}	8.4	1.5	8.0	216	1.1	41.4	14.8	251

[†] Leading number refers to constraining dataset used in the inversion. “A” indicates that all crack data were used in the inversion, while “B” denotes the subset of data used (subset 1, 2 or 3). Appended “u” indicates uniform strain magnitude assumed for all constraining data, “d” indicates a denser-spaced element mesh, and “x” indicates models including the supplementary postulated data point at 22°S.

[‡] Number of elements.

[§] Moment is defined as the modulus of rigidity (3×10^{10} N/m²) times the sum of the slip times area of all fault patches.

[#] Mean azimuth of the element slip vector projected onto the half-space surface. The mean value is weighted by the slip magnitude.

^{††} Angular difference between the mean observed crack strike in each cluster and calculated most compressional principal stress axis at the cluster location.